Chinese Chemical Letters 37 (2026) 111664

Contents lists available at ScienceDirect

Chinese Chemical Letters

journal homepage: www.elsevier.com/locate/cclet

An efficient and stable protonic ceramic fuel cell cathode achieved by Yb-doping

Yixuan Huang, Jiacheng Zeng, Wenjie Gong, Wanbin Lin, Hao Liu, Chuqian Jian, Xiaofeng Chen, Tang Sheng, Li Zhang, Fan He, Yu Chen*

School of Environment and Energy, State Key Laboratory of Luminescent Materials and Devices, Guangdong Provincial Key Laboratory of Atmospheric Environment and Pollution Control, South China University of Technology, Guangzhou 510006, China

ARTICLE INFO

Article history:
Received 19 June 2025
Revised 30 July 2025
Accepted 31 July 2025
Available online 5 August 2025

Keywords:
Cathode
Protonic ceramic fuel cells
Oxygen reduction reaction
Ytterbium doping
Stability

ABSTRACT

With high fuel flexibility, high energy efficiency, and low carbon emissions, protonic ceramic fuel cells (PCFCs) have been recognized as a promising energy conversion device. However, the sluggish oxygen reduction reaction (ORR) kinetics occurring at the cathodes significantly hinder the further development of PCFCs. Herein, a Yb-doped cathode material based on $PrBaCo_2O_{5+\delta}$ (PBC) perovskite with a nominal composition of $PrBaCo_{1.95}Yb_{0.05}O_{5+\delta}$ ($PBCYb_{0.05}$) is reported. The $PBCYb_{0.05}$ is made up of two phases, which are deficient-$PrBa_{1-x}Co_{1.95-0.99x}Yb_{0.05-0.1x}O_{5+\delta}$ (D-$PBCYb_{0.05}$) major phase and $BaCo_{0.99}Yb_{0.01}O_{3-\delta}$ (BCYO) secondary phase, demonstrating a low area-specific resistance of 0.249 Ω cm^2 and commendable electrocatalytic stability at 600 °C. In comparison to PBC, the $PBCYb_{0.05}$ exhibits accelerated oxygen transport kinetics and higher oxygen vacancy concentration, confirmed by the analyses of electrical conductivity relaxation and X-ray photoelectron spectroscopy. When implemented as the air electrode in PCFCs, $PBCYb_{0.05}$ delivers an outstanding peak power density (PPD) of 2.25 W/cm^2 at 700 °C, representing a high enhancement over undoped PBC cells.

© 2026 Published by Elsevier B.V. on behalf of Chinese Chemical Society and Institute of Materia Medica, Chinese Academy of Medical Sciences.

The extensive adoption of renewable energy is essential for the attainment of sustainable development [1]. Protonic ceramic fuel cells (PCFCs), as a new generation of clean energy devices, have become a focal point in recent green energy research owing to their high fuel utilization, low cost, and excellent sustainability [2–5]. However, the widespread development of PCFCs is still constrained by the limited kinetics of the oxygen reduction reaction (ORR) and insufficient durability of cathodes [6–9]. Consequently, for the practical implementation of PCFCs, it is imperative to develop cathodes with both high electrocatalytic activity for ORR and exceptional durability under operating conditions [10,11]. The structural versatility of perovskite-type oxides, resulting from their tunable cationic substitution of A and B sites, creates dynamic redox active sites and controllable oxygen vacancy concentrations [12]. These properties make them highly attractive as cathode materials for PCFCs. So far, $La_{0.6}Sr_{0.4}Co_{0.2}Fe_{0.8}O_{3-\delta}$ (LSCF), $Ba_{0.5}Sr_{0.5}Co_{0.8}Fe_{0.2}O_{3-\delta}$ (BSCF), $BaCo_{0.4}Fe_{0.4}Zr_{0.1}Y_{0.1}O_{3-\delta}$ (BCFZY), *etc.*, representing the perovskite-type oxides, have been extensively applied in PCFCs and achieved outstanding electrochemical performance [13–15]. $PrBaCo_2O_{5+\delta}$ (PBC), a conventional air electrode material with mixed ionic and electronic conductivity, enables remarkable electrocatalytic activity for ORR and superior oxygen diffusion kinetics [16,17]. The segregation of Ba at the A-site in the PBC cathode induces the stability of PCFCs during operation [18,19]. Therefore, it is necessary to employ targeted modification strategies to improve the structural integrity and electrochemical performance of PBC for effective integration.

Various practicable methodologies were applied to further improve the electro-catalytic activity and structural integrity of the PBC-based cathodes. For example, Gao *et al.* infiltrated a multi-cationic oxide catalyst coating with a composition of $Pr_{0.2}Ce_{0.2}Ni_{0.2}Co_{0.2}Fe_{0.2}O_x$ (PCNCF) to boost the ORR activity and longevity of the PBC cathode [20]. The PCNCF-coated PBC air electrode achieved more satisfactory fuel cell performance than the bare PBC air electrode at 700–600 °C. Meanwhile, as the cerium oxide in the catalyst coating reacted with separate Ba to form active ingredients, both the catalytic reaction activity and the operational stability of PBC have been improved [20]. Entropy engineering can endow perovskite oxides with multifunctionality, including electrocatalytic activity, phase stability, and rapid ion transport [21]. Zhu *et al.* modulated the conformational entropy of the PBC perovskite by doping alkaline earth metals at the A-site to develop a medium-entropy $Pr_{0.5}Ba_{1/6}Sr_{1/6}Ca_{1/6}CoO_{5+\delta}$ (PBSCC)

* Corresponding author.
E-mail address: eschenyu@scut.edu.cn (Y. Chen).

https://doi.org/10.1016/j.cclet.2025.111664
1001-8417/© 2026 Published by Elsevier B.V. on behalf of Chinese Chemical Society and Institute of Materia Medica, Chinese Academy of Medical Sciences.

electrode with enhanced functionality [22]. The PCFCs incorporating the PBSCC cathode demonstrated exceptional performance (0.80 W/cm^2 at 550 °C) and stability (for over 250 h) [23]. In addition, precisely engineered doping with cations has been considered as a widely adopted modification strategy to improve ORR activity and reinforce structural robustness for PBC [24]. Du *et al*. adopted an In-doping method to develop a $PrBa_{0.95}Co_{1.85}In_{0.09}O_{5+\delta}$ (PBCIn) air electrode with a $BaCo_{0.85}In_{0.15}O_{3-\delta}$ (BCIO) cubic second phase [25]. Indium doping has been demonstrated to enhance ORR and OER kinetics, enabling the PBCIn air electrodes to achieve remarkable electrochemical performance (1.33 W/cm^2 at 600 °C) in PCFCs [25].

Recently, lanthanide elements have been extensively utilized as dopants in PCFCs. Ytterbium, an element in the lanthanide series, has attracted considerable attention [26,27]. Yb doping has been widely proven as an effective strategy for developing advanced proton-conducting electrolytes [28]. Yang *et al*. reported that $BaZr_{0.1}Ce_{0.7}Y_{0.2-x}Yb_xO_{3-\delta}$ (BZCYYb), a Y and Yb co-doped mixed ion conductor, enabled rapid transport of protons and oxide ion vacancies, achieving high ionic conductivity at 700–500 °C [29]. Further, Guo *et al.* discovered that higher Yb doping levels led to a simultaneous rise in proton concentration and ionic conductivity, suggesting a critical role of Yb in BZCYYb [30]. Luo *et al*. synthesized a Yb-doped $BaHf_{0.1}Ce_{0.7}Yb_{0.2}O_{3-\delta}$ (BHCYb172) proton-conducting electrolyte, which has high ionic conductivity and excellent chemical stability [31]. When applied in PCFCs, the cell showed outstanding performance of 1.73 W/cm^2 at 600 °C, caused by the fact that Yb doping can increase oxygen migration rates and reduce both activation energy and thermal expansion coefficient in diverse crystalline materials [32–34]. To date, studies on the substitution of Yb are primarily focused on electrolytes, with limited investigation of their application in the cathodes of PCFCs. Due to the lower valence state, Yb^{3+} doping at the B-site may increase the oxygen vacancy concentration [31]. These intrinsic vacancies could promote water incorporation to provide proton sources that contribute to the charge transfer process on the electrode surfaces [35]. Furthermore, in perovskites, the Gibbs free energy of hydration exhibits a linear dependence on the average cationic electronegativity, with lower electronegativity favoring stronger water adsorption [36,37]. The substitution of Co with lower-electronegativity Yb^{3+} at the B-site could enhance hydration capability, consequently improving electrocatalytic activity. Studies are showing that doping with low-electronegativity elements effectively improved the performance of PBC air electrodes, such as $PrBa_{0.9}Cs_{0.1}Co_2O_{5+\delta}$ (PBCsC) and $PrBaCo_{1.8}Nb_{0.1}Y_{0.1}O_{5+\delta}$ (PBCNY) [38,39].

Inspired by the above findings, we designed a ytterbium-doped PBC-based perovskite material with the designed composition of $PrBaCo_{1.95}Yb_{0.05}O_{5+\delta}$ ($PBCYb_{0.05}$). The perovskite consists of a major perovskite phase of deficient-$PrBa_{1-x}Co_{1.95-0.99x}Yb_{0.05-0.01x}O_{5+\delta}$ (D-$PBCYb_{0.05}$) and a minor secondary perovskite phase $BaCo_{0.99}Yb_{0.01}O_{3-\delta}$ (BCYO). The nanoscale synergy between these two phases significantly enhances both the electrocatalysis and durability of the cathode. From the results of the experiments, compared to the PBC, $PBCYb_{0.05}$ displays more oxygen vacancies and faster oxygen surface exchange and bulk conduction kinetics. Therefore, the $PBCYb_{0.05}$ cathode achieved a relatively low area-specific resistance of 0.249 Ω cm^2 (*vs.* 0.410 Ω cm^2 from the PBC). The PCFCs employing the developed $PBCYb_{0.05}$ cathode achieved an outstanding power density of 2.25 W/cm^2 at 700 °C and a desirable short-term stability for 103 h at 600 °C.

The details of chemicals and materials, material preparation, cell fabrication, electrochemical measurements, and characterization of materials are provided in Supporting information.

To characterize the phase composition of $PBCYb_{0.05}$, we performed the X-ray diffraction (XRD) and related Rietveld refinement analysis. As shown in Fig. 1a, the $PBCYb_{0.05}$ powder is composed of a major perovskite phase of deficient-$PrBa_{1-x}Co_{1.95-0.99x}Yb_{0.05-0.01x}O_{5+\delta}$ (D-$PBCYb_{0.05}$, $a = b = 3.888$ Å and $c = 7.705$ Å, 95.08 wt%) and a minor secondary perovskite phase of $BaCo_{0.99}Yb_{0.01}O_{3-\delta}$ (BCYO, $a = b = c = 4.143$ Å, 4.92 wt%). The corresponding fitting parameters are $R_{wp} = 4.02$ %, $R_p = 3.06$ %, and $\chi^2 = 2.008$, indicating that the Rietveld refinement analysis is reasonable. XRD patterns of PBC and other materials with Yb doping ratios are given in Fig. 1b and Fig. S1 (Supporting information). The BCYO secondary phase emerges when the Yb doping ratio is 1.25 %, and its volume fraction increases significantly at 2.50 %. The heterogeneous phase increases when the Yb content reaches 3.75 %. It is worth noting that the main characteristic peak of $PBCYb_{0.05}$ exhibits a distinct shift to a lower angle at 32°−34°, compared to PBC, suggesting a lattice expansion (Fig. S2 in Supporting information). This phenomenon indicates that ytterbium has successfully been doped into the B-site of the PBC perovskite since the ionic radius of Yb^{3+} is between the Pr^{3+}/Pr^{4+} and Co^{3+}/Co^{4+} [38–40]. It has been confirmed that Yb preferentially occupies the B-sites of perovskites containing large A-site elements such as Pr, Ba, and Sr [41]. The chemical compatibility between the $PBCYb_{0.05}$ powder and $BaZr_{0.1}Ce_{0.7}Y_{0.1}Yb_{0.1}O_{3-\delta}$ (BZCYYb) powder is illustrated in Fig. S3 (Supporting information). The result indicates there are no chemical side reactions between the $PBCYb_{0.05}$ air electrode and the BZCYYb electrolyte. To determine the phase composition of $PBCYb_{0.05}$, HR-TEM was employed in combination with energy-dispersive spectroscopy (EDS) mapping analysis. Distinct regions of $PBCYb_{0.05}$ and BCYO can be identified in the HR-TEM image (Fig. 1c). As shown in Fig. 1d, the lattice spacing of BCYO, determined by fast Fourier transformation (FFT), is approximately 0.207 nm, likely corresponding to the (002) crystallographic plane. Analogously, the measured lattice spacing of 0.276 nm matches mostly with the (110) crystallographic plane of $PBCYb_{0.05}$ through FFT (Fig. 1e). From the STEM and EDS mapping images, the absence of the Pr element is visible (Fig. 1f). The SEM images of the $PBCYb_{0.05}$ and PBC powders are shown in Figs. S4 and S5 (Supporting information). In contrast, the BCYO nanoparticles can be found in $PBCYb_{0.05}$. Combined with the other results (XRD and TEM), it is demonstrated that $PBCYb_{0.05}$ is a two-phase composite with D-$PBCYb_{0.05}$ and BCYO.

Electrochemical impedance spectroscopy (EIS) curves of BZCYYb electrolyte-supported symmetrical cells with $PrBaCo_{2-x}Yb_xO_{5+\delta}$ ($x = 0$, 0.05, 0.10, and 0.15) (denoted as PBC, $PBCYb_{0.05}$, $PBCYb_{0.10}$, $PBCYb_{0.15}$) electrodes are performed to evaluate the Yb doping effect on the electrochemical performance of PBC-based electrodes (Fig. 2a and Fig. S6-S8 in Supporting information). All the EIS curves were measured at an open-circuit voltage (OCV) condition in humid air (3 vol% H_2O). The area-specific resistance (ASR) values of the $PBCYb_{0.05}$ symmetrical electrode are 0.077, 0.150, 0.249, 0.441, and 1.013 Ω cm^2 at 700, 650, 600, 550, and 500 °C, respectively. As exhibited in Fig. 2b, the $PBCYb_{0.05}$ electrode achieves the minimum ASR among all Yb doping ratios, suggesting that the formation of unitary and pure BCYO secondary phase is crucial for electrochemical performance. The enhanced electrochemical performance after ytterbium doping compared to the PBC electrode may be attributed to the relatively lower electronegativity of Yb^{3+}, which can reduce the average electronegativity of cations in the system. As evidenced by the ASR comparison in Fig. 2c, the $PBCYb_{0.05}$ air electrode exhibits remarkable electrocatalytic performance relative to reported advanced cathodes, demonstrating its superior catalytic activity [13,21,23,39,42–45]. Further details of these cells are in Table S2 (Supporting information). Meanwhile, the electrochemical stability of symmetrical cells is also an important index for evaluating the cathode. As shown in Fig. 2d, the electrochemical stabilities of symmetrical cells with $PBCYb_{0.05}$ and PBC cathode are measured in humid air (3 vol% H_2O) at 600 °C.

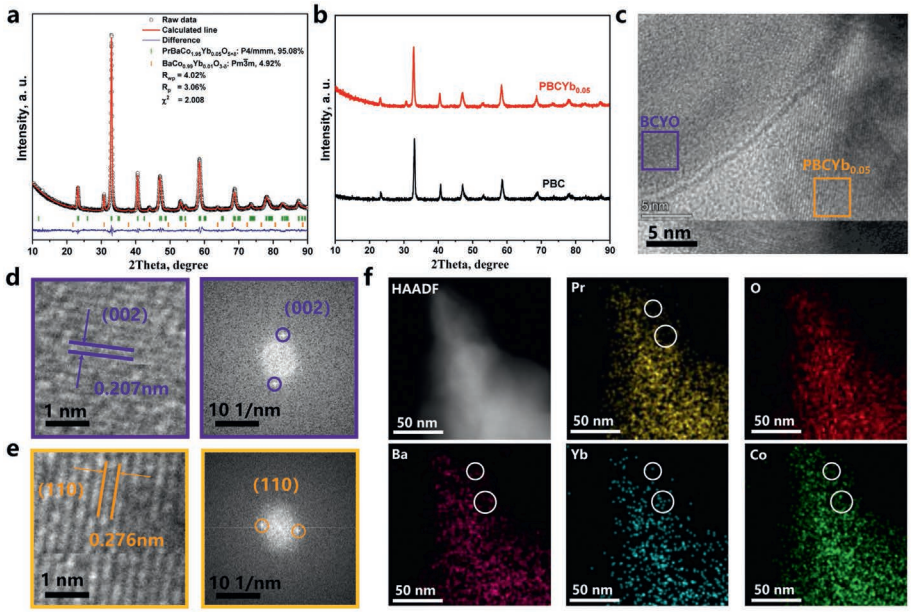


Fig. 1. Phase characterization of the $PBCYb_{0.05}$ powder. (a) XRD Rietveld refinement of $PBCYb_{0.05}$ powder sintered at 1000 °C for 4 h. (b) XRD patterns of $PBCYb_{0.05}$ and PBC powders sintered at 1000 °C for 4 h. (c) HR-TEM images of $PBCYb_{0.05}$ powder. The lattice spacings and FFT images of (d) BCYO and (e) $PBCYb_{0.05}$. (f) STEM image and EDS mapping of $PBCYb_{0.05}$ powder with Pr, O, Ba, Yb, and Co elements.

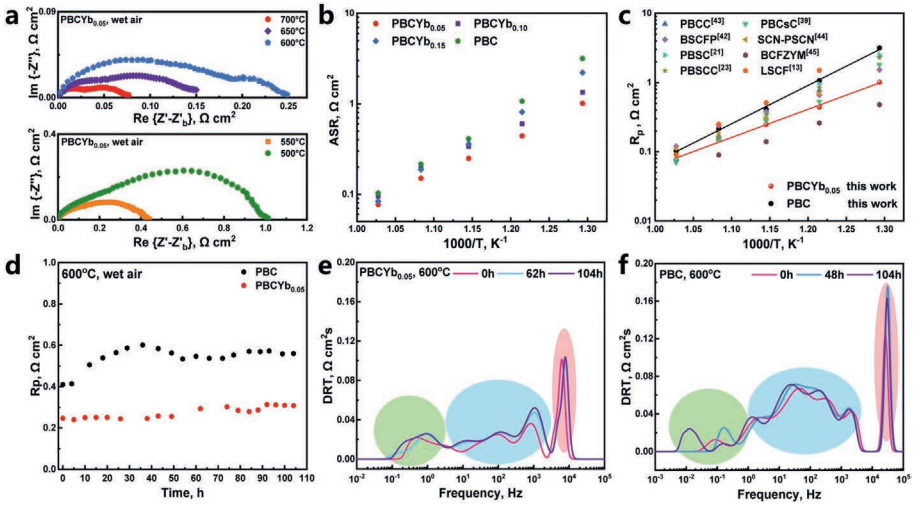


Fig. 2. Cathode performance in symmetrical cells. (a) EIS curves of BZCYYb electrolyte-supported symmetrical cells with $PBCYb_{0.05}$ air electrode tested in humid air (3 vol% H_2O) at 700–500 °C. (b) Electrocatalytic performance comparison of symmetrical cells with $PBCYb_{0.10}$, $PBCYb_{0.05}$, PBC, and $PBCYb_{0.15}$ electrodes. (c) Area-specific resistance of $PBCYb_{0.05}$ and PBC in this work relative to other materials recently reported. (d) Short-term stability of a symmetrical cell with $PBCYb_{0.05}$ air electrode in humid air (3 vol% H_2O) at 600 °C. The DRT curves of symmetrical cells with (e) $PBCYb_{0.05}$ and (f) PBC air electrodes during stability testing.

The corresponding EIS spectra are presented in Figs. S9 and S10 (Supporting information), respectively. The polarization resistance (R_p) values of the $PBCYb_{0.05}$ air electrode increased from 0.249 Ω cm^2 to 0.308 Ω cm^2 for 104 h, indicating that it maintained better stability than the PBC air electrode (from 0.410 Ω cm^2 to 0.506 Ω cm^2 for 104 h). The electrochemical performance stability of the $PBCYb_{0.10}$ air electrode with the corresponding EIS curves is also tested (Figs. S11 and S12 in Supporting information). After 104 h of operation, the R_p values of the $PBCYb_{0.10}$ air electrode finally ended at 0.355 Ω cm^2, exceeding the final R_p values of $PBCYb_{0.05}$. The result highlights the better electrochemical stability of the $PBCYb_{0.05}$ air electrode. To elucidate the degradation mechanisms of symmetrical cells, the distribution of relaxation times (DRT), a deconvolution method to resolve EIS curves into discrete electrochemical processes, was applied. Three distinct electrochemical processes can be resolved in a DRT spectrum through different frequency distributions: Low frequency (LF, 10^{-3}–10 Hz), intermediate frequency (IF, 10–10^4 Hz), and high frequency (HF, 10^4–10^5 Hz). Three typical EIS curves from the stability measurements of the $PBCYb_{0.05}$ and PBC cathodes are selected for the DRT analysis, covering the beginning, the middle, and the end. As shown in Fig. 2e, the change in DRT curves is concentrated in the IF range, suggesting that the processes of oxygen surface exchange primarily govern the R_p evolution in the $PBCYb_{0.05}$ air electrode [46]. Similarly, the increased R_p values of the PBC air electrode originate from modifications in both LF and HF ranges (Fig. 2f). The LF and HF ranges are associated with gas diffusion and charge transfer processes, respectively [46–48]. The results confirm the efficacy of Yb^{3+} doping in improving gas diffusion and charge transfer efficiency.

The underlying mechanism for the superior electrochemical performance of the $PBCYb_{0.05}$ air electrode requires thorough exploration. The electrical conductivities of $PBCYb_{0.05}$ and PBC

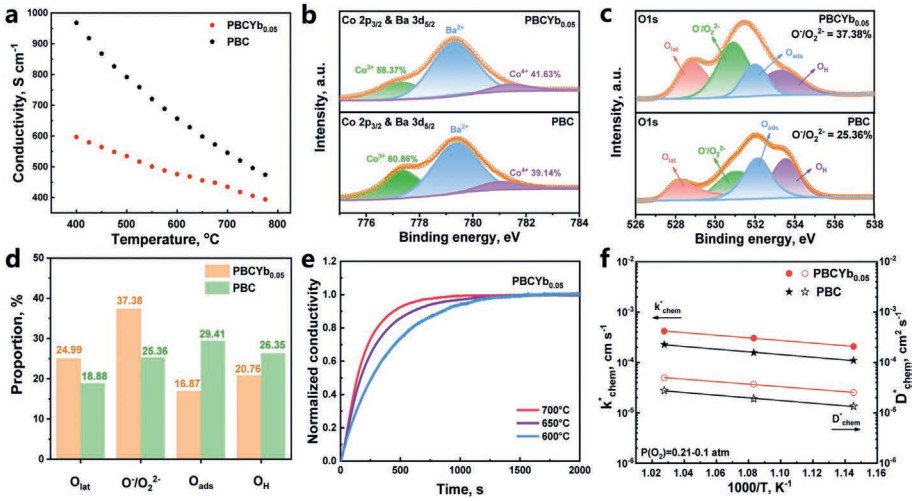


Fig. 3. Discussion on the mechanism of the $PBCYb_{0.05}$ electrode. (a) Electrical conductivity of $PBCYb_{0.05}$ and PBC samples from 400 °C to 775 °C. (b) The Co $2p_{3/2}$, Ba $3d_{5/2}$ and (c) O 1s XPS spectra for PBC and $PBCYb_{0.05}$ powders. (d) Column distribution of four oxygen species in $PBCYb_{0.05}$ *vs.* PBC powders. (e) ECR response curves of $PBCYb_{0.05}$ sample from 700 °C to 600 °C. (f) Temperature dependence of the k^*_{chem}/D^*_{chem} for $PBCYb_{0.05}$ and PBC samples.

samples are shown in Fig. 3a. Both samples exhibit the same temperature-dependent conductivity trend as reported in the literature, showing a decrease in conductivity with increasing temperature. Compared to the PBC sample, the relatively low conductivity of the $PBCYb_{0.05}$ sample originates from the substitution of Yb at Co sites, breaking the strongly covalent Co-O bonds [49]. The surface chemistry of PBC and $PBCYb_{0.05}$ powders was characterized by XPS to determine Co valence states and oxygen vacancy concentration. As displayed in Fig. 3b, according to the binding energies, the Co $2p_{3/2}$ and Ba $3d_{5/2}$ XPS spectra can be classified into three subsidiary peaks: Co^{3+} (central peak is at ≈777.15 eV), Ba^{2+} (central peak is at ≈779.29 eV), and Co^{4+} (central peak is at ≈780.89 eV) [22]. After Yb^{3+} doping, the rise in Co^{4+} content implies greater catalytic activity availability [50]. Likewise, the O 1s XPS spectra can be resolved into four distinct peaks, which are the lattice oxygen (O_{lat}, central peak is at ≈528.75 eV), the highly oxidative oxygen (O^-/O_2^{2-}, central peak is at ≈531.01 eV), the adsorbed oxygen (O_{ads}, central peak is at ≈531.94 eV) and the hydroxyl oxygen (O_H, central peak is at ≈533.37 eV) (Fig. 3c) [25]. The relative distribution percentages of four distinct peaks for $PBCYb_{0.05}$ and PBC materials are quantified in Fig. 3d. The oxygen vacancy concentration correlates with the value of O^-/O_2^{2-}. A higher value of highly oxidative oxygen of $PBCYb_{0.05}$ ($O^-/O_2^{2-} = 37.38\%$) than that of PBC ($O^-/O_2^{2-} = 25.36\%$) may suggest that Yb doping can lead to more oxygen vacancies in the cathode [25]. To provide additional evidence of the improvement in oxygen transport kinetics and ORR activity, we measured the electrical conductivity relaxation (ECR) response curves of both $PBCYb_{0.05}$ and PBC samples from 700 °C to 600 °C (Fig. 3e and Fig. S13 in Supporting information). The determination of surface exchange coefficients (k^*_{chem}) and bulk diffusion coefficients (D^*_{chem}) is based on Fick's second law. As exhibited in Fig. 3f, the k^*_{chem} and D^*_{chem} values of $PBCYb_{0.05}$ are larger than those of PBC, revealing that the oxygen surface exchange and diffusion kinetics of the $PBCYb_{0.05}$ cathode are enhanced [8]. The detailed k^*_{chem} and D^*_{chem} are listed in Table S3 (Supporting information). These experimental data confirm that the ORR activity of the PBC-based air electrode can be improved by effectively accelerating the oxygen transport kinetics through Yb doping. Thus, incorporating an appropriate amount of Yb into PBC perovskite generates multifunctional improvements, leading to superior electrocatalytic activity. In addition, thermal expansion coefficient (TEC) curves of the $PBCYb_{0.05}$ and PBC samples are exhibited in Fig. S14 (Supporting information). It is shown that $PBCYb_{0.05}$ exhibits a similar thermal expansion to other cobalt-based electrode materials [21,51,52].

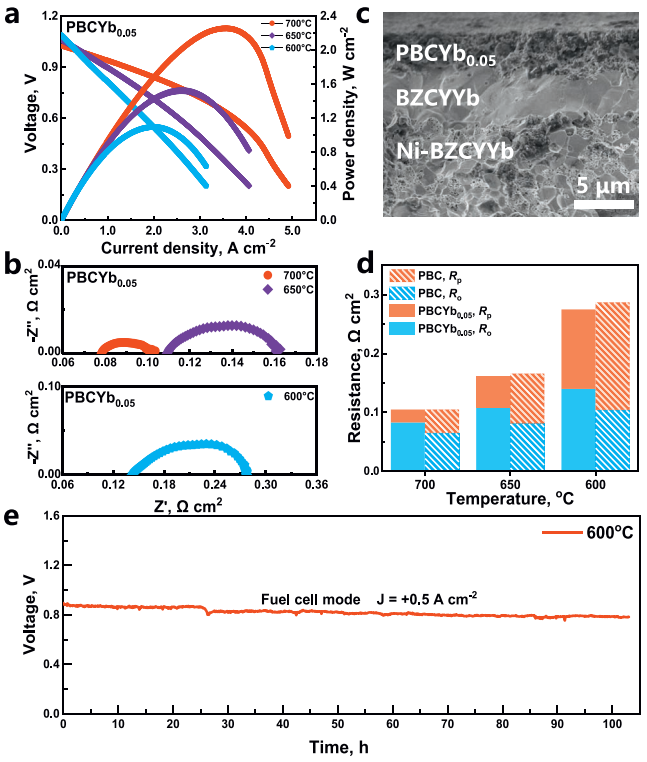


Fig. 4. Electrochemical performance and microcosmic structure of PCFCs loaded with $PBCYb_{0.05}$ and PBC cathodes. (a) The *I-V-P* curves and (b) impedance spectra of PCFCs loaded with $PBCYb_{0.05}$ cathode from 700 °C to 600 °C. (c) The cross-sectional SEM image of a single cell loaded with the $PBCYb_{0.05}$ cathode after electrochemical testing. (d) Comparison of R_o and R_p of PCFCs loaded with $PBCYb_{0.05}$ and PBC cathodes. (e) Operational durability of $PBCYb_{0.05}$ cell at a current density of 0.5 A/cm^2 and 600 °C.

The Ni-BZCYYb anode-supported PCFCs with $PBCYb_{0.05}$ or PBC cathode were assembled and systematically tested for electrochemical performance and durability to verify the improvement in ORR activity and oxygen transport. As depicted in Fig. 4a, the current density-voltage-power density (*I-V-P*) curves of the PCFC

Table 1
Comparison of the PPDs of $PBCYb_{0.05}$ and PBC cells with other recently reported cells which possess a similar construction.

Air electrode	Electrolyte	Fuel electrode	Electrolyte thickness (μm)	Temp. (°C)	PPD (W/cm^2)	Source
$PrBaCo_{1.95}Yb_{0.05}O_{5+\delta}$ ($PBCYb_{0.05}$)	BZCYYb	Ni-BZCYYb	~7	700	2.25	This work
				650	1.52	
				600	1.09	
$PrBaCo_2O_{5+\delta}$ (PBC)	BZCYYb	Ni-BZCYYb	~7	700	1.68	This work
				650	1.22	
				600	0.96	
$Pr_{0.1}Ce_{0.9}O_{2+\delta}$-$PrBaCo_2O_{5+\delta}$ (PCO-PBC)	BZCYYb	Ni-BZCYYb	8	700	1.77	[10]
				650	1.21	
				600	0.87	
$Pr_{0.5}Ba_{0.5}Co_{0.7}Fe_{0.25}Sn_{0.05}O_{3-\delta}$ (PBCFS05)	BZCYYb	Ni-BZCYYb	6–7	700	1.64	[53]
				650	1.33	
				600	1.12	
$PrBaCo_{1.92}Zr_{0.08}O_{5+\delta}$ (PBCZ)	BZCYYb	Ni-BZCYYb	15	700	1.45	[54]
				650	0.99	
				600	0.55	
$SrCo_{0.5}Nb_{0.5}O_{3-\delta}$-$Pr_{0.5}Sr0_{.5}Co_{0.9}Nb_{0.1}O_{3-\delta}$ (SCN-PSCN)	BZCYYb	Ni-BZCYYb	~10	700	1.78	[44]
				650	1.36	
				600	0.89	
$BaCe_{0.25}Fe_{0.75}O_{3-\delta}-0.75V_2O_3$ (BCF-V75)	BZCYYb	Ni-BZCYYb	~20	700	2.04	[55]
				650	1.73	
				600	1.21	
$PrBa_{0.8}Ca_{0.2}Co_2O_6$ (PBCC)	BZCYYb	Ni-BZCYYb	8	700	1.69	[56]
				650	1.22	
				600	0.88	
$PrBa_{0.8}Ca_{0.2}Co_{1.95}Pd_{0.05}O_{5+\delta}$ (PBCCPd)	BZCYYb	Ni-BZCYYb	8	700	2.08	[43]
				650	1.41	
				600	0.97	
$PrBa_{0.8}Ca_{0.2}Fe_{1.8}Ce_{0.2}O_{6-\delta}$ (PBCFC)	BZCYYb	Ni-BZCYYb	10	700	1.78	[57]
				650	1.27	
				600	0.87	
$PrBaCo_{1.9}In_{0.1}O_{5+\delta}$ ($PBCIn_{0.10}$)	BZCYYb	Ni-BZCYYb	8	700	2.25	[25]
				650	1.78	
				600	1.33	
$PrBaCo_{1.8}Nb_{0.1}Y_{0.1}O_{5+\delta}$ (PBCNY)	BZCYYb	Ni-BZCYYb	~8	700	1.99	[38]
				650	1.44	
				600	0.97	

loaded with the $PBCYb_{0.05}$ air electrode are measured during fuel cell operation from 700 °C to 600 °C. Remarkable peak power densities (PPDs) of 2.25, 1.52, and 1.09 W/cm^2 are achieved at 700, 650, and 600 °C, respectively. Simultaneously, as shown in Fig. 4b, under OCV conditions, the R_p values of this PCFC remain relatively low, which are 0.022, 0.054, and 0.135 Ω cm^2 at 700, 650, and 600 °C, respectively. After electrochemical testing under hydrogen reduction conditions, the cross-sectional scanning electron microscopy (SEM) image of this PCFC is presented in Fig. 4c. The specific morphologies of the $PBCYb_{0.05}$ air electrode and Ni-BZCYYb fuel electrode are exhibited in Figs. S15 and S16 (Supporting information). The PCFC possesses a classic triple-layer structure, consisting of a porous $PBCYb_{0.05}$ air electrode layer (≈6 μm), a dense BZCYYb electrolyte layer (≈7 μm), and a porous Ni-BZCYYb fuel electrode layer. To enable direct comparison, the *I-V-P* curve and area-specific polarization resistances of the PCFC loaded with PBC air electrode are recorded in Figs. S17 and S18 (Supporting information). The PCFC loaded with PBC air electrode exhibits peak power densities of 1.68, 1.22, and 0.96 W/cm^2 at 700, 650, and 600 °C, respectively. The enhanced electrochemical performance can be attributed to the Yb doping in PBC. Meanwhile, at 700, 650, and 600 °C, the R_p values of the PCFC loaded with PBC air electrode are 0.040, 0.085, and 0.183 Ω cm^2, respectively. The electrochemical resistances, including both ohmic resistances (R_o) and R_p of PCFCs loaded with $PBCYb_{0.05}$ and PBC cathode, are quantitatively compared in Fig. 4d. Although the R_o of the PCFC with $PBCYb_{0.05}$ air electrode is marginally larger, the significantly lower R_p values compared to those with the PBC air electrode are responsible for the enhanced power output, suggesting the polarization resistance of PCFCs contributes mostly to the performance improvement. To explore the influence of different Yb-doped cathodes on the performance of PCFCs, the *I-V-P* curves and the corresponding impedance spectra of PCFCs loaded with $PBCYb_{0.10}$ and $PBCYb_{0.15}$ cathodes were measured (Figs. S19-S22 in Supporting information). Among all the Yb-doped cathodes, the PCFC loaded with $PBCYb_{0.05}$ exhibited the best electrochemical performance, as demonstrated by the test results of symmetrical cells. In recent literature, the performance of the $PBCYb_{0.05}$ cell has surpassed most of its counterparts with comparable electrolyte architectures (Table 1 and Fig. S23 in Supporting information) [10,25,38,43,44,53–57]. As shown in Fig. 4e, at a current density of 0.5 A/cm^2 and 600 °C, the PCFC loaded with $PBCYb_{0.05}$ air electrode maintained stable operation for 103 h with a slight degradation rate of 1.08 mV/h, demonstrating the Yb-doped PBC enables reliable application as cathode in PCFCs.

To summarize, we have successfully developed a Yb-doped PBC-based air electrode with a nominal composition of $PBCYb_{0.05}$. As evidenced by XRD patterns, HR-TEM images, and EDS mapping, the coexistence of D-PBCY and BCYO phases in the $PBCYb_{0.05}$ material is confirmed. According to the testing of symmetrical cells and DRT analysis, the $PBCYb_{0.05}$ air electrode demonstrates excellent electrocatalytic activity and operational stability. From the combined analyses of XPS and ECR, compared to PBC, $PBCYb_{0.05}$ possesses more oxygen vacancies and faster oxygen transport kinetics, accounting for enhanced oxygen reduction reaction (ORR) activity. In the single-cell tests, the PCFCs loaded with $PBCYb_{0.05}$ cathode achieved an ideal peak power density of 2.25 W/cm^2 at 700 °C. In addition, it also showed promising durability for 103 h during operation. The testing demonstrates that the Yb-doped PBC serves as a highly reliable air electrode for the practical applications of PCFCs. The Yb-doping strategy efficiently broadens the modification methodologies for the cathodes in PCFCs.

CRediT authorship contribution statement

Yixuan Huang: Writing – original draft, Visualization, Investigation, Data curation. **Jiacheng Zeng:** Software, Investigation, Data curation. **Wenjie Gong:** Investigation, Data curation. **Wanbin Lin:** Investigation, Data curation. **Hao Liu:** Investigation, Data curation. **Chuqian Jian:** Investigation, Data curation. **Xiaofeng Chen:** Investigation, Data curation. **Tang Sheng:** Investigation, Data curation. **Li Zhang:** Investigation, Data curation. **Fan He:** Investigation, Data curation. **Yu Chen:** Writing – review & editing, Project administration, Funding acquisition, Conceptualization.

Declaration of competing interest

The authors declare that they have no known competing financial interests or personal relationships that could have appeared to influence the work reported in this paper.

Acknowledgments

This work was financially supported by the National Natural Science Foundation of China (No. 22179039), the Guangdong Basic and Applied Basic Research Foundation (No. 2024A1515010448), the Introduced Innovative R&D Team of Guangdong (No. 2021ZT09L392), the Pearl River Talent Recruitment Program (No. 2019QN01C693), the Zijin Mining Group Co., Ltd. (No. 5405–ZC–2023–00008), and Guangzhou Applied Basic Research Plan Project (No. 2024A04J3079).

Supplementary materials

Supplementary material associated with this article can be found, in the online version, at doi:10.1016/j.cclet.2025.111664.

References

[1] S.W. Boettcher, Chem. Rev. 124 (2024) 13095.
[2] H. Ding, W. Wu, C. Jiang, et al., Nat. Commun. 11 (2020) 1907.
[3] Z. Wang, Y. Wang, J. Wang, et al., Nat. Catal. 5 (2022) 777.
[4] N. Wang, C. Tang, L. Du, et al., Adv. Energy Mater. 12 (2022) 2201882.
[5] S. Jiang, X. Zheng, W. Sun, Adv. Energy Mater. 15 (2024) 2403745.
[6] P. Yao, J. Zhang, Q. Qiu, et al., Adv. Energy Mater. 15 (2024) 2403335.
[7] S. Zhao, W. Ma, B. He, et al., Adv. Mater. 37 (2025) 2501387.
[8] P. Qiu, B. Liu, L. Wu, et al., J. Adv. Ceram. 11 (2022) 1988.
[9] J. Sun, R. Ren, H. Yue, et al., Chin. Chem. Lett. 34 (2023) 107776.
[10] K. Pei, S. Luo, F. He, et al., Appl. Catal. B 330 (2023) 122601.
[11] N. Han, R. Ren, M. Ma, et al., Chin. Chem. Lett. 33 (2022) 2658.
[12] M. Humayun, Z. Li, M. Israr, et al., Chem. Rev. 125 (2025) 3165.
[13] Y. Zhou, W. Zhang, N. Kane, et al., Adv. Funct. Mater. 31 (2021) 2105386.
[14] Z. Shao, S.M. Haile, Nature 431 (2004) 170.
[15] C. Duan, D. Hook, Y. Chen, J. Tong, R. O'Hayre, Energy Environ. Sci. 10 (2017) 176.
[16] D. Wang, Y. Xia, H. Lv, et al., Int. J. Hydrog. Energy 45 (2020) 31017.
[17] K. Zhang, L. Ge, R. Ran, Z. Shao, S. Liu, Acta Mater. 56 (2008) 4876.
[18] B. Wei, M. Schroeder, M. Martin, ACS Appl. Mater. Interfaces 10 (2018) 8621.
[19] L. Zhu, B. Wei, Z. Lü, et al., Appl. Surf. Sci. 416 (2017) 649.
[20] H. Gao, F. He, F. Zhu, et al., Adv. Funct. Mater. 34 (2024) 2401747.
[21] F. He, Y. Zhou, T. Hu, et al., Adv. Mater. 35 (2023) 2209469.
[22] F. Zhu, Z. Du, K. Xu, et al., Adv. Energy Mater. 14 (2024) 2401048.
[23] F. Zhu, M. Hou, Z. Du, et al., Energy Environ. Sci. 17 (2024) 7782.
[24] W. Zhang, Y. Zhou, E. Liu, et al., Appl. Catal. B 299 (2021) 120631.
[25] Z. Du, K. Xu, F. Zhu, et al., Adv. Funct. Mater. 34 (2024) 2409188.
[26] I. Cho, J. Yun, B. Seong, et al., J. Energy Chem. 88 (2024) 1.
[27] N. Danilov, E. Pikalova, J. Lyagaeva, et al., J. Power Sources 366 (2017) 161.
[28] S.A. Ismail, D. Han, J. Am. Ceram. Soc. 105 (2022) 7548.
[29] L. Yang, S. Wang, K. Blinn, et al., Science 326 (2009) 126.
[30] H. Guo, Y. Li, L. Jiang, et al., J. Mater. Chem. A 12 (2024) 5875.
[31] Z. Luo, Y. Zhou, X. Hu, et al., Energy Environ. Sci. 15 (2022) 2992.
[32] M. Zhu, R. Zhou, C. Tian, et al., Ceram. Int. 51 (2025) 1699.
[33] A. Aguadero, M.J. Martínez-Lope, V. Pomjakushin, J.A. Alonso, Eur. J. Inorg. Chem. 2011 (2011) 3226.
[34] A.P. Anantharaman, H.P. Dasari, Ceram. Int. 47 (2021) 4367.
[35] K. Xu, H. Zhang, Y. Xu, et al., Adv. Powder Mater. 3 (2024) 100187.
[36] R. Zohourian, R. Merkle, G. Raimondi, J. Maier, Adv. Funct. Mater. 28 (2018) 1801241.
[37] K. Park, M. Saqib, H. Lee, et al., Energy Environ. Sci. 17 (2024) 1175.
[38] Y. Huang, F. He, K. Xu, et al., Adv. Funct. Mater. 34 (2024) 2409598.
[39] Y. Xu, K. Xu, F. Zhu, et al., ACS Energy Lett. 8 (2023) 4145.
[40] S. Tanabe, K. Hirao, N. Soga, J. Am. Ceram. Soc. 75 (2005) 503.
[41] X. Hu, Y. Zhou, Z. Luo, et al., Energy Environ. Sci. 17 (2024) 9335.
[42] Z. Liu, D. Cheng, Y. Zhu, et al., Chem. Eng. J. 450 (2022) 137787.
[43] Z. Du, F. He, H. Gao, et al., Energy Storage Mater. 68 (2024) 103345.
[44] C. Fang, Y. Huang, K. Xu, et al., J. Power Source 614 (2024) 234984.
[45] M. Liang, Y. Song, D. Liu, et al., Appl. Catal. B 318 (2022) 121863.
[46] J.H. Kim, K. Jang, D.K. Lim, et al., J. Mater. Chem. A 10 (2022) 2496.
[47] Z. Liu, Y. Lin, H. Nie, et al., Adv. Funct. Mater. 34 (2023) 2311140.
[48] Y. Chen, S. Yoo, Y. Choi, et al., Energy Environ. Sci. 11 (2018) 2458.
[49] T. Xia, N. Lin, H. Zhao, et al., J. Power Source 192 (2009) 291.
[50] F. He, Q. Gao, Z. Liu, et al., Adv. Energy Mater. 11 (2021) 2003916.
[51] K. Liu, F. Lu, X. Jia, et al., J. Mater. Chem. A 10 (2022) 24410.
[52] X. Liu, X. Xi, Y. Liao, et al., Appl. Catal. B 359 (2024) 124509.
[53] M. Fu, W. Hu, H. Tong, et al., J. Adv. Ceram. 13 (2024) 63.
[54] X. Zhang, R. Song, D. Huan, et al., Small 18 (2022) 2205190.
[55] S. Tang, M. Fu, Z. Qin, Y. Gao, Z. Tao, Adv. Funct. Mater. 35 (2025) 2501995.
[56] T. Hu, Y. Xu, K. Xu, F. Zhu, Y. Chen, SusMat 3 (2023) 91.
[57] T. Hu, F. Zhu, J. Xia, et al., Adv. Funct. Mater. 33 (2023) 2305567.